







Quantum spin mixing in Dirac materials

Ying-Jiun Chen ^{1,2✉}, Markus Hoffmann ³, Bernd Zimmermann³, Gustav Bihlmayer ³, Stefan Blügel ³,
Claus M. Schneider ^{1,2,4} & Christian Tusche ^{1,2✉}

The spin of the electron is nowadays replacing the charge as basic carrier of information not only in spintronics applications, but also in the emerging field of quantum information. Topological quantum materials, where spin-momentum locking is believed to lead to particularly long spin lifetimes, are regarded as a promising platform for such applications. However, spin-orbit coupling, that is essential to all topological matter, at the same time gives rise to spin mixing and decoherence as a major obstacle for quantum computing. Here, we give experimental evidence that hot-spots of spin-mixing and spin-conserving contributions of the spin-orbit operator coexist in an archetypal topological Dirac metal, and that these hot spots can have a strongly anisotropic distribution of their respective wave vectors with respect to the spin quantization direction. Our results can be understood within a theory that takes into account the decomposition of the spin-orbit Hamiltonian into spin-conserving and spin-flip terms, contributing to a better understanding of quantum decoherence in topological materials, in general.

¹Peter Grünberg Institut (PGI-6), Forschungszentrum Jülich, Jülich, Germany. ²Fakultät für Physik, Universität Duisburg-Essen, Duisburg, Germany. ³Peter Grünberg Institut and Institute for Advanced Simulation, Forschungszentrum Jülich and JARA, Jülich, Germany. ⁴Department of Physics, University of California Davis, Davis, CA, USA. ✉email: yi.chen@fz-juelich.de; c.tusche@fz-juelich.de

In spintronic devices, the spin of the electron becomes the main carrier of information, providing a link between magnetism and conventional charge-based electronics. In this approach, spin-up (\uparrow) and spin-down (\downarrow) states of the electron spin serve as a classical bit to represent and store binary information^{1,2}. On the microscopic level, however, the electron spin by its nature has a quantum mechanical origin. As a consequence, the statistical interpretation of quantum mechanics provides possibilities to find the eigenvalue $\frac{\hbar}{2}$ and $-\frac{\hbar}{2}$ for spins pointing up and down along a given quantization axis. In particular, any given spin state can be represented as a superposition,

$$|\psi\rangle = a|\uparrow\rangle + b|\downarrow\rangle, \quad (1)$$

of these two states. Quantum physics therefore allows information to be represented and processed in a significantly different manner, beyond the classical interpretation of spintronics. In this picture of spin-based quantum computing, the coherent superposition of two distinct spin states represents a single quantum bit, a so-called qubit^{2,3}.

A fundamental mechanism that allows the control of the electron spin in condensed matter is provided by spin-orbit coupling (SOC). Due to SOC, the eigenstates of the Hamiltonian are no longer wave functions with a pure spin character, but a superposition of up and down states. This manifests in a manifold of phenomena. On the one side, SOC is the source of spin-momentum locking found in the electronic structure of topological quantum materials, leading to particularly long spin lifetimes. By contrast, the mixture of spin-up and spin-down states due to SOC enables that scattering events will flip the spin of an electron with a certain probability. For instance, the Elliott–Yafet spin-relaxation mechanism, being driven by SOC, represents a major source of spin decoherence^{2,4,5}.

To understand this apparent discrepancy, the SOC operator can be divided into a spin-conserving $\xi(L_S S_S)^{\uparrow\uparrow}$ and a spin-flip $\xi(L_S S_S)^{\uparrow\downarrow}$ part:

$$\xi \mathbf{L} \cdot \mathbf{S} = \xi(L_S S_S)^{\uparrow\uparrow} + \xi(L_S S_S)^{\uparrow\downarrow}. \quad (2)$$

For a fixed direction of the spin quantization axis (SQA), these two contributions correspond to states with a pure spin character and fully spin-mixed states, respectively. Here, ξ is the strength of SOC, \mathbf{L} and \mathbf{S} are the orbital and spin angular momentum operators, $L_S = \mathbf{L} \cdot \hat{s}$, $S_S = \mathbf{S} \cdot \hat{s}$, and \hat{s} is a unit vector in the direction of the SQA. As the spin-orbit operator is a non-local operator, it depends on the energy and wave vector of the respective states. In crystalline solids, thus, the electronic structure can have regions in the Brillouin zone (BZ) of particularly large spin relaxation. Such regions have, for instance, direct consequences in the interpretation of ultrafast dynamics of spin-dependent properties^{1,5–10}. A direct experimental access to the contrasting contributions of SOC in the electronic structure has so far remained elusive. Yet, such information would help to identify spots of long/short spin lifetime and might pave the way towards a precise control of spin states via on-demand tailoring of the SOC.

Here we used spin- and momentum-resolved photoelectron spectroscopy to map the SOC spin-mixing parameter in the Fermi surface (FS) of the prototypical heavy transition metal tungsten (W). Tungsten has the highest charge- to spin-current conversion efficiency among all 5d transition metals, suggesting a significant role of SOC in its FS topology^{11–15}. We have investigated the twofold rotational symmetric (C_{2v}) W(110) surface. In reminiscence of a crystalline topological insulator, the mirror symmetry of W(110) leads to several *d*-orbital-derived surface states with a helical spin texture^{16–19}. The W(110) surface thus represents a paradigmatic model system to understand the non-local distribution of spin-conserving and spin-mixing parts of the

SOC operator in the electronic structure. Our experimental and theoretical results give direct evidence that spin mixing in the W (110) surface becomes strongly anisotropic, with a pronounced non-uniform distribution of spin-mixing hotspots in the FS. Our results have important consequences for spintronics and understanding the efficiency of spin-torques and spin-current generation, as well as spin-coherence effects in quantum materials.

Results

Multiple *d*-derived Dirac fermions in W(110). Figure 1a presents the layout of our spin-resolved momentum microscopy experiments. Photoelectrons are collected simultaneously over the full solid angle above the sample, allowing the efficient measurement of the spin-resolved spectral function over the complete surface BZ (SBZ) (see ‘Methods’)^{20–22}. The momentum image shows the electronic states at the Fermi energy E_F .

Figure 1b–d show sections through the electronic structure between E_F and $E_F - 1.7$ eV. The W(110) surface is known to host in total three gapless points in the SBZ forming Dirac cones with linear dispersion: one appears at the centre and two are away from the high-symmetry points of the SBZ^{17–19}. In our measurements, we can clearly observe all three Dirac cones in the SBZ. Their positions are summarized in Fig. 1e. These three Dirac cones can be classified into two sets with distinct group velocities: one at the $\bar{\Gamma}$ point and two at $k_y = \pm 0.4 \text{ \AA}^{-1}$. They are located inside a spin-orbit-induced bulk band gap that resembles the formation of the Dirac-cone surface band inside the fundamental gap of a topological insulator¹⁷. The linear bands cross at the $\bar{\Gamma}$ point at $E_B = 1.25$ eV (see Fig. 1b, c). At $k_y = \pm 0.4 \text{ \AA}^{-1}$, the Dirac point lies at $E_B = 0.75$ eV, as shown in Fig. 1d. The presence of an odd number of gapless Dirac cones indicates a non-trivial topological character. Tungsten has been therefore classified as a *d*-orbital-derived topological crystalline material¹⁶ where the Dirac cones are protected by the mirror symmetry of the (110) surface.

Full spin texture. Because of the combination of the twofold surface symmetry and time-reversal symmetry, the out-of-plane component of spin polarization vanishes at all k -points in W (110)²³, i.e., $P_z = 0$. A negligible out-of-plane spin polarization is further confirmed by our first-principle calculations. As a result, the initial-state spin polarization is purely in-plane, with components P_x and P_y . During the photoemission by linearly polarized light, additional contributions to the spin polarization may arise due to the lowered symmetry by the incidence direction of the light, as discussed in detail in refs. 24,25. Here we chose a geometry where the SQA lies within the optical plane, such that these effects are minimized (see ‘Methods’) and the measured spin polarization is expected to closely reflect the W(110) FS spin texture. In particular, when the W(110) surface is excited with linearly polarized light, a purely in-plane spin polarization has been previously reported, whereas a non-zero P_z component can be obtained using circularly polarized light²⁶.

Figure 2a shows the measured spin-resolved FS contour of W (110) for a vertical P_y in-plane polarization, the same spin direction as discussed in Fig. 1. The measured FS contour agrees well with previous results that have probed P_y ¹⁸. In particular, we find a high polarization reaching P_y values up to ± 0.7 in the pronounced cross-shaped contour. These states can be related to *d*-orbital-derived surface resonances²⁷. The spin-resolved measurement reveals that a Rashba-like spin splitting is found around the $\bar{\Gamma}$ point (A), whereas the vertical contour of the FS (B) at $k_y = \pm 0.4 \text{ \AA}^{-1}$ merge into the off-centred Dirac cone observed in Fig. 1d. The ellipse-shaped contours around the \bar{S} points are surface states that exhibit a small Rashba-like spin splitting.

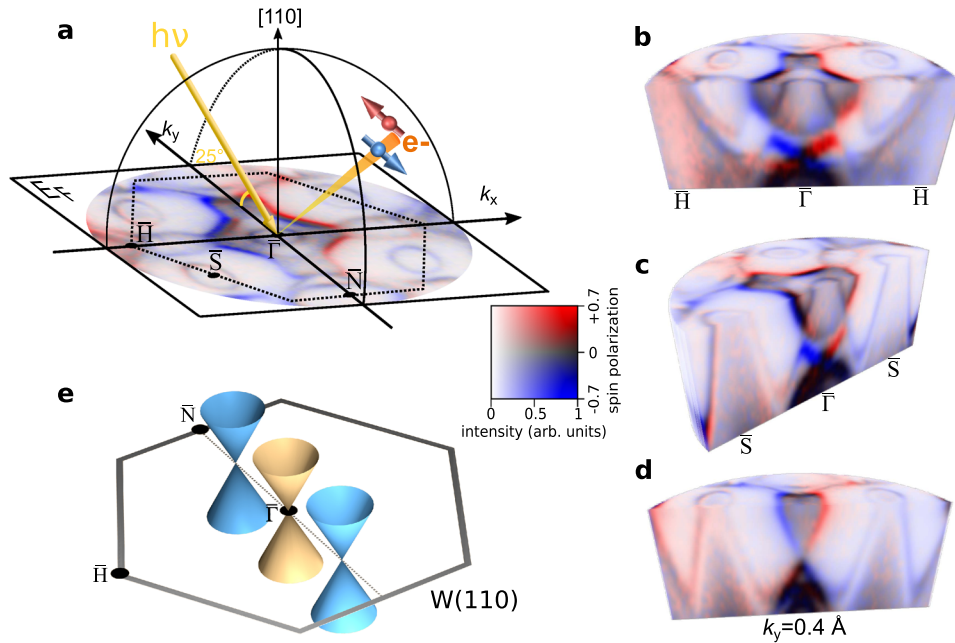


Fig. 1 Multiple *d*-derived Dirac fermions in the heavy transition metal W(110). **a** Experimental geometry for spin- and momentum-resolved photoelectron study. The spin-resolved photoemission momentum map at the Fermi energy E_F for W(110) is shown. The dashed contour indicates the outline of the surface Brillouin zone of W(110), together with the high-symmetry points ($\bar{\Gamma}$, \bar{H} , \bar{N} , \bar{S}). **b-d** Full 3D (k_x, k_y, E_B) spin-resolved momentum map with a photon energy of $h\nu = 50$ eV, cutting along $\bar{H} - \bar{\Gamma} - \bar{H}$ (**b**), $\bar{S} - \bar{\Gamma} - \bar{S}$ (**c**), and $k_y = 0.4 \text{ \AA}^{-1}$ (**d**) directions of W(110) as a function of binding energies E_B ($E - E_F$ from 0 to -1.7 eV). Measured intensities and spin polarization are encoded using the displayed 2D colour code, where the spin polarization P_y is indicated by red and blue colours, and the colour saturation encodes the intensity. **e** Schematic of the three observed Dirac states for W(110): one appears at the $\bar{\Gamma}$ point and two coexist at $k_y = \pm 0.4 \text{ \AA}^{-1}$.

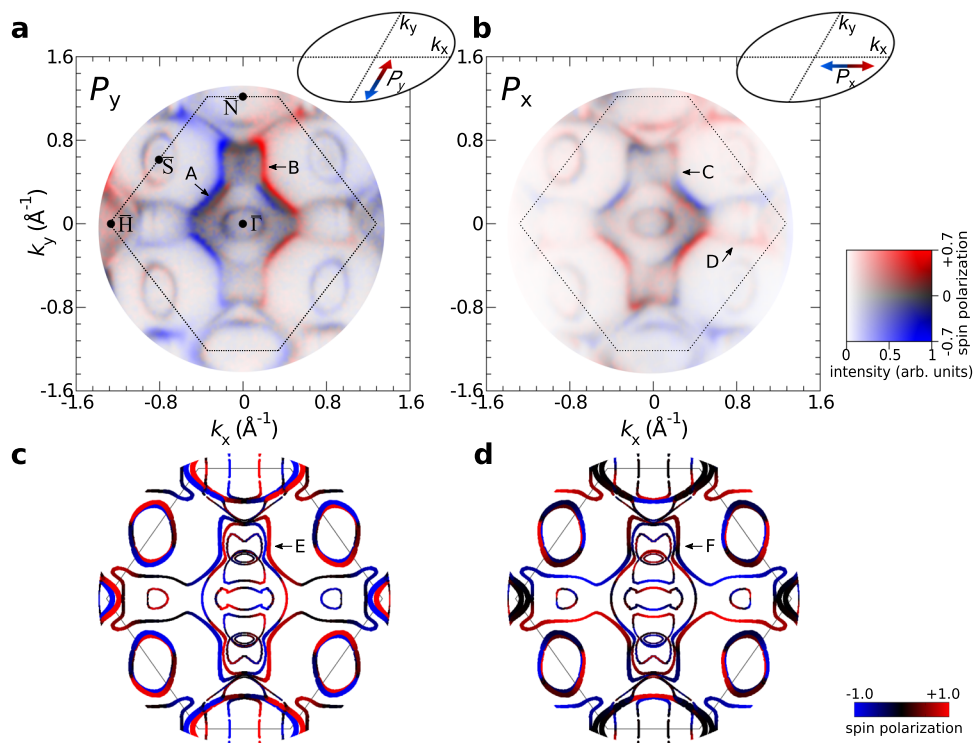


Fig. 2 Full spin texture. **a, b** Measured spin-resolved Fermi surface (FS) of W(110). Measured intensities and spin polarization are encoded using the displayed 2D colour code, where the spin polarization P_y (**a**) or P_x (**b**) is indicated by red and blue colours, respectively, and the colour saturation encodes the intensity. **c, d** Theoretical spin-resolved FS of W(110). Colours indicate the in-plane spin component along the k_y (**c**) or k_x (**d**) direction. Letters A-F indicate distinguished features in the FS contour with high/low spin polarization as a guide to the eye.

A significant change of the spin polarization is found for the P_x component in Fig. 2b: in general, P_x changes the sign upon the mirror operation $k_y \rightarrow -k_y$, but is unchanged upon $k_x \rightarrow -k_x$. This reflects the fact that the spin angular momentum described by pseudovectors fulfils time-reversal and mirror symmetries. The overall magnitude of the measured P_x only reaches values of ± 0.5 and is significantly reduced compared to P_y . In particular, P_x vanishes along the vertical sections of the main FS contour (C) at $k_y \approx \pm 0.4 \text{ \AA}^{-1}$ and only small polarizations are observed along the horizontal sections (D). This provides already a qualitative picture of the in-plane spin texture: the spin is locally aligned tangential to the FS contour, in reminiscence of the spin warping observed in some topological insulators rather than being locked normal to the k -vector as in a regular Rashba model.

Figure 2c, d show the theoretical spin-resolved FS for P_y and P_x , respectively. The calculation reproduces the main details of the experiment, in particular the P_x and P_y spin polarizations along the cross-shaped FS contour. As in the experiment, the maximum polarization is observed in the P_y component along the vertical sections in vicinity of the off-centred Dirac cone (E), whereas P_x vanishes for these states (F). Furthermore, we clearly observe the Rashba-splitting of the surface states around the \bar{S} points. The calculation further confirms the experimental observation that both P_x and P_y , at the same time, show a strongly reduced polarization along the vertical $k_x = 0$ mirror plane of W(110). The quantitative overall agreement between theory and experiments confirms that our measured results mainly represent the initial-state spin polarization.

Figure 3a shows the spin texture over the whole SBZ. As discussed above, in the outer contour of the cross-like feature, spin-momentum locking leads to a counterclockwise rotation around the BZ centre. At larger binding energies, these states converge into the Dirac-cone states. The two nearly degenerate ellipse-shaped surface states around \bar{S} are very close to each other. The Rashba-like opposite spin chirality explains the low observed spin polarization for P_x and P_y (see Fig. 2a, b).

Anisotropic quantum spin mixing. Due to the helical spin texture, one would anticipate a similarly high degree of spin polarization for the P_x and P_y momentum maps. For instance, this would be the expected case for the spin texture of an archetypal Rashba surface state with isotropic free-electron-like bands. Such model systems are the L -gap surface states on the (111) faces of noble metals like Au(111)²⁰. In contrast, we find a pronounced dependence of the observed spin polarization on the choice of the SQA: the overall spin polarization P_x is substantially suppressed, compared to P_y . To understand the underlying mechanism of how the choice of the SQA of an incoming conduction electron affects the degree of spin polarization, we carried out ab initio calculations⁵ to analyse the momentum distribution of the spin-mixing parameter.

Figure 3b, c show the theoretical momentum-resolved spin-mixing parameters b_{bs}^2 (see ‘Methods’)⁵ of the W(110) FS when the SQA points along the y and x axes, respectively. A fully spin-mixed state ($b_{bs}^2 = \frac{1}{2}$) is represented by a superposition of $|\uparrow\rangle$ and $|\downarrow\rangle$ spin states with a probability of 0.5. As a spin-resolved measurement integrates over an ensemble of many observed electrons, spin-mixing hot areas (red colours in Fig. 3) consequently appear with no effective spin polarization in the experiment. Likewise, a pure spin state corresponds to $b_{bs}^2 = 0$ and results in a high spin polarization (positive or negative) along the respective SQA. The measured spin-polarization maps in Fig. 2a, b thus provide a direct experimental access to the distribution of the spin-mixing parameter in the SBZ.

By rotating the SQA from the y - to the x -axis, the spin mixing varies considerably. With the SQA $\parallel y$, spin mixing is relatively uniform over the FS. A few hotspots of large spin mixing are located at places of large band curvature and along the vertical $k_x = 0$ plane. This picture changes dramatically when the SQA $\parallel x$. In the latter case, full spin mixing is prominent in large areas of the SBZ. In these regions, the Bloch wave functions become a superposition of spin-up and spin-down states of the same magnitude.

This result is in perfect agreement with our experimental observations in Fig. 2b, where an overall low spin polarization is found. If an electron is scattered into such states, there is a high probability that the spin flips. They thus represent a source of decoherence, degrading the ability of qubits and spintronics to retain encoded information. As a consequence, the strong spin mixing gives rise to hot areas of enhanced spin flip when the SQA points along the x -, but not when the SQA points along the y -direction.

Discussion

Due to SOC, the spin and orbital character of the Bloch states depends strongly on the spin orientation with respect to the crystal axes. This leads to drastic changes in the spin-conserving $\xi(L_S S_S)^{\uparrow\uparrow}$ and a spin-mixing $\xi(L_S S_S)^{\uparrow\downarrow}$ part of the electronic states with respect to the choice of the SQA. We note that the total SOC term (Eq. (2)) is a scalar product, which is independent of the SQA. This representation thus allows us to describe the anisotropic distribution of spin mixing in the entire BZ. In particular, a large $\xi(L_S S_S)^{\uparrow\downarrow}$ indicates a mixing of spin states due to the presence of SOC.

The distribution of the spin mixing in the BZ has immediate consequences for spin dynamics and spin-related properties^{1,5–10}. For instance, in regions of the BZ where the spin-conserving part of SOC is dominant, the electron spin is protected from dissipative effects, giving rise to relatively long spin lifetimes. The spin information of these states is thus preserved, being useful when a long spin lifetime is needed in spintronic devices and

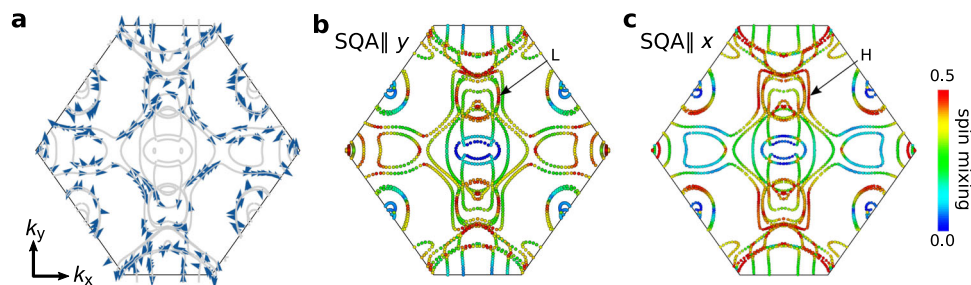


Fig. 3 Anisotropic spin mixing. **a** Theoretical full spin texture of W(110). **b, c** Theoretical momentum-resolved spin-mixing parameters b_{bs}^2 on the Fermi surfaces of W(110) for the spin quantization axis (SQA) along y (**b**) and x (**c**) axes. Blue colours represent a pure spin character of the Bloch states along the SQA, whereas red colours indicate a fully mixed spin state, where spin-up and spin-down electrons are found with an equal probability of 0.5.

quantum information applications. On the other hand, regions with an enhanced spin-mixing will have a major contribution to spin-relaxation processes and ultrafast spin dynamics.

Although the eigenenergies of the Bloch states are independent of the SQA, the choice of the SQA can alter the momentum distribution of spin-conserving and spin-mixing contributions. For simplicity, spin relaxation as it is described by the Elliott–Yafet mechanism^{2,4} does not take into account these individual relaxation hotspots in the BZ. Nevertheless, it has been shown that the macroscopic Elliott–Yafet relaxation parameter can be obtained directly by integrating the wave-vector-dependent spin-relaxation parameter from Fig. 3b, c over the BZ⁵. The wave vector of the respective electron states, however, becomes of importance in single-crystalline materials and junctions, where tunnelling currents, spin-dependent excitations, and spin–orbit torque are selectively driven by small areas in the FS of the materials^{1,5,14,28,29}. Spin-conserving and spin-mixing contributions thus are dominated by hotspots in the FS and can be exploited by appropriately designed devices.

Our findings show that the spin mixing of the Bloch states in a non-magnetic material can change drastically when the spin quantization direction varies. As a consequence, the spin-mixing parameter becomes strongly anisotropic. The Dirac surface states, marked by H, serve as the main source of anisotropy, with the spin-mixing parameter changing by >50% between SQA||*x* and SQA||*y*. This result can be attributed to strong spin-momentum locking perpendicular to the *k_x* momentum direction. In contrast, the states marked by L show almost no anisotropy. A large spin mixing for both SQAs is here mediated by a strong overlap with the projected bulk bands²⁷.

The spin-mixing parameter introduced here is a direct consequence of the superposition principle of quantum mechanics. Our observations confirm experimentally the possibility to visualize the effect of a superposition of quantum mechanical wave functions, namely the spin-up and spin-down states that form a mixed spin state due to a strong SOC. We demonstrate the potential scope of spin-momentum locking for quantum spin-mixing manipulation in Dirac materials. Our findings are widely applicable in abundant crystals with SOC and offer promising perspectives to fine-tune the quantum (de)coherence within one material by changing the spin polarization of a conduction electron in a spintronic device.

Methods

Spin-resolved momentum microscopy. Spin- and momentum-resolved photoelectron spectroscopy experiments were carried out at the NanoESCA beamline³⁰ of the Elettra synchrotron in Trieste (Italy), using *p*-polarized photons at the photon energy $h\nu = 50$ eV. All measurements were performed while keeping the sample at a temperature of 130 K. Photoelectrons emitted into the complete solid angle above the sample surface were collected using a momentum microscope^{20,22}. The momentum microscope directly forms an image of the distribution of photoelectrons as a function of the lateral crystal momentum (*k_x*, *k_y*) that is recorded on an imaging detector^{20,22}.

An imaging spin filter based on the spin-dependent reflection of low-energy electrons at a W(100) single crystal³¹ allows the simultaneous measurement of the spin polarization of photoelectrons in the whole SBZ. Images were recorded after reflection at a scattering energy at 26.5 and 30.5 eV, which changes the spin sensitivity *S* of the detector between 42% and 5%, respectively. From these images, the spin polarization at every (*k_x*, *k_y*) point in a momentum map at certain binding energies (e.g., Figs. 1 and 2 in the main study) is derived^{21,31,32}. As a *d*-orbital-derived topological metal, sizable photoemission intensities of the Dirac states are mainly observed by excitation with *p*-polarized light³³. As verified by our first-principles calculations (see Fig. 2c, d), our measurements using *p*-polarized light reproduce well the ground-state spin polarization, such that pronounced effects by optical orientation, which are observed for *p*-orbital topological materials, only play a minor role^{34,35}.

The spin-resolved momentum microscopy measurements were performed along the quantization axis of the spin filter, being the same direction as $\bar{\Gamma} - \bar{N}$, *k_y* of W(110). In order to measure the transverse component of the spin polarization parallel to the *k_x* ($\bar{\Gamma} - \bar{H}$) direction of W(110), we rotated the sample around 90°. The *k_x* direction of the sample then is parallel to the quantization axis of the spin

filter (see Fig. 2 of the main manuscript). In this way, the SQAs for the measurements of the *P_x* and *P_y* components always lie within the optical plane, such that time-reversal and mirror symmetries of the spin polarization are preserved.

The W(100) crystal of the spin filter was prepared by following the same procedure as described below for W(110). This standard procedure is known to lead to clean tungsten surfaces^{31,32}. The spin-resolved photoemission momentum maps for each constant energy contour, as shown in Fig. 1a, were measured only for 6 min. This allows to collect spin-resolved data in a wide range of binding energies, *E_B*. The complete 3D (*k_x*, *k_y*, *E_B*) information of the spin-resolved spectral function is obtained within a 2 h measurement time. Despite many attempts, it has not been possible so far to achieve a comparably detailed information by conventional spin-resolved photoemission spectroscopy³⁶.

Cleaning procedure for a tungsten single crystal. The procedure for cleaning W(110) consists of two steps: (i) cycles of low-temperature flash heating (*T* ~ 1200 K) at an oxygen partial pressure of *P_{O₂}* = 5 × 10^{−8} mbar to remove the carbon from the surface and (ii) a single high-temperature flash (*T* ~ 2400 K) to remove the oxide layer³². The cleanliness of the W(110) surface was checked by low-energy electron diffraction and Auger electron spectroscopy.

First-principles calculations. Using the full-potential linearized augmented-plane-wave method as implemented in the FLEUR code (<http://www.flapw.de>), we performed density functional theory calculations of 7 layers of W(110). We adopted the structural parameters given by Heide et al.³⁷. Exchange and correlation effects were treated within the local-density approximation (LDA)³⁸. The spin–orbit interaction was included self-consistently and the spin quantization direction was chosen with respect to $\bar{\Gamma} - \bar{N}$ and $\bar{\Gamma} - \bar{H}$ directions of W(110). The plane-wave cutoff was chosen as *k_{max}* = 4.2 *a₀*^{−1} with *a₀* as Bohr’s radius and the muffin-tin radii set to 2.5 *a₀*.

To determine the FS with high precision, we calculated the eigenspectrum on a dense uniform mesh of 256 × 256 *k*-points in the full BZ. The Fermi-level crossings were then obtained by triangulation. To improve the agreement with experiment, we shifted the position of the Fermi level in our calculations downwards by 70 meV as compared to the theoretical value for the Fermi energy.

Our investigation for the momentum distribution of the spin-mixing parameter is based on density functional calculation within the LDA³⁹. We employ the full-potential Korringa–Kohn–Rostoker Green function method⁴⁰ with exact treatment of the atomic cell shapes^{41,42}. After a self-consistent full-potential calculation performed within the scalar-relativistic approximation, SOC is added when calculating the FS properties⁴³. The spin-mixing parameter is given by

$$b_{\text{ss}}^2 = 1/2 - \langle S_y \rangle_k / \hbar. \quad (3)$$

Wave functions are chosen in a way that the spin (*S_y*) along the SQA \hat{s} is maximized. *b_{ss}*² can then obtain values between 0 (pure spin state) and 1/2 (fully mixed spin state). Usually, the Bloch states are of nearly pure spin character. However, at special spin flip hotspots in the BZ spin mixing may increase significantly up to 1/2, which corresponds to the case of fully spin-mixed states.

Data availability

The data that support the findings of this study are available from the corresponding author upon reasonable request.

Received: 7 February 2021; Accepted: 19 July 2021;

Published online: 11 August 2021

References

1. Sinova, J. & Žutić, I. New moves of the spintronics tango. *Nat. Mater.* **11**, 368 (2012).
2. Awschalom, D. D., Bassett, L. C., Dzurak, A. S., Hu, E. L. & Petta, J. R. Quantum spintronics: engineering and manipulating atom-like spins in semiconductors. *Science* **339**, 1174–1179 (2013).
3. Preskill, J. Quantum computing in the NISQ era and beyond. *Quantum* **2**, 79 (2018).
4. Murakami, S., Nagaosa, N. & Zhang, S.-C. Dissipationless quantum spin current at room temperature. *Science* **301**, 1348–1351 (2003).
5. Zimmermann, B. et al. Anisotropy of spin relaxation in metals. *Phys. Rev. Lett.* **109**, 236603 (2012).
6. Fabian, J. & Das Sarma, S. Spin relaxation of conduction electrons in polyvalent metals: theory and a realistic calculation. *Phys. Rev. Lett.* **81**, 5624–5627 (1998).
7. Soumyanarayanan, A., Reyren, N., Fert, A. & Panagopoulos, C. Emergent phenomena induced by spin–orbit coupling at surfaces and interfaces. *Nature* **539**, 509 (2016).

8. Kurebayashi, H. et al. An antidamping spin-orbit torque originating from the Berry curvature. *Nat. Nanotechnol.* **9**, 211– (2014).
9. Seifert, T. S. et al. Femtosecond formation dynamics of the spin seebeck effect revealed by terahertz spectroscopy. *Nat. Commun.* **9**, 2899 (2018).
10. Siegrist, F. et al. Light-wave dynamic control of magnetism. *Nature* **571**, 240–244 (2019).
11. Wang, M. et al. Current-induced magnetization switching in atom-thick tungsten engineered perpendicular magnetic tunnel junctions with large tunnel magnetoresistance. *Nat. Commun.* **9**, 671– (2018).
12. Sheng, P. et al. The spin Nernst effect in tungsten. *Sci. Adv.* **3**, e1701503 (2017).
13. Pai, C.-F. et al. Spin transfer torque devices utilizing the giant spin hall effect of tungsten. *Appl. Phys. Lett.* **101**, 122404 (2012).
14. Cho, S., Baek, S.-h.C., Lee, K.-D., Jo, Y. & Park, B.-G. Large spin hall magnetoresistance and its correlation to the spin-orbit torque in W/CoFeB/MgO structures. *Sci. Rep.* **5**, 14668 (2015).
15. Kim, D.-J. et al. Observation of transverse spin nernst magnetoresistance induced by thermal spin current in ferromagnet/non-magnet bilayers. *Nat. Commun.* **8**, 1400 (2017).
16. Zhang, T. et al. Catalogue of topological electronic materials. *Nature* **566**, 475 (2019).
17. Varykhalov, A. et al. Tilted dirac cone on W(110) protected by mirror symmetry. *Phys. Rev. B* **95**, 245421 (2017).
18. Kutnyakhov, D. et al. Spin texture of time-reversal symmetry invariant surface states on W(110). *Sci. Rep.* **6**, 29394 (2016).
19. Miyamoto, K. et al. Spin-polarized Dirac-cone-like surface state with *d* character at W(110). *Phys. Rev. Lett.* **108**, 066808 (2012).
20. Tusche, C., Krasnyuk, A. & Kirschner, J. Spin resolved bandstructure imaging with a high resolution momentum microscope. *Ultramicroscopy* **159**, 520–529 (2015).
21. Tusche, C. et al. Nonlocal electron correlations in an itinerant ferromagnet. *Nat. Commun.* **9**, 3727 (2018).
22. Tusche, C., Chen, Y.-J., Schneider, C. M. & Kirschner, J. Imaging properties of hemispherical electrostatic energy analyzers for high resolution momentum microscopy. *Ultramicroscopy* **206**, 112815 (2019).
23. Mirhosseini, H., Giebels, F., Gollisch, H., Henk, J. & Feder, R. Ab initio spin-resolved photoemission and electron pair emission from a Dirac-type surface state in W(110). *N. J. Phys.* **15**, 095017 (2013).
24. Heinzmann, U. & Dil, J. H. Spin-orbit-induced photoelectron spin polarization in angle-resolved photoemission from both atomic and condensed matter targets. *J. Phys. Condens. Matter* **24**, 173001 (2012).
25. Osterwalder, J. Can spin-polarized photoemission measure spin properties in condensed matter? *J. Phys. Condens. Matter* **24**, 171001 (2012).
26. Miyamoto, K., Wortelen, H., Okuda, T., Henk, J. & Donath, M. Circular-polarized-light-induced spin polarization characterized for the Dirac-cone surface state at W(110) with C_{2v} symmetry. *Sci. Rep.* **8**, 10440 (2018).
27. Elmers, H. J. et al. Hosting of surface states in spin-orbit induced projected bulk band gaps of W(110) and Ir(111). *J. Phys. Condens. Matter* **29**, 255001 (2017).
28. Tusche, C. et al. Oxygen-induced symmetrization and structural coherency in Fe/MgO/Fe(001) magnetic tunnel junctions. *Phys. Rev. Lett.* **95**, 176101 (2005).
29. Tusche, C. et al. Tusche et al. reply. *Phys. Rev. Lett.* **96**, 119602 (2006).
30. Wiemann, C. et al. A new nanospectroscopy tool with synchrotron radiation: Nanoesca@Elettra. *e-J. Surf. Sci. Nanotechnol.* **9**, 395–399 (2011).
31. Tusche, C. et al. Spin resolved photoelectron microscopy using a two-dimensional spin-polarizing electron mirror. *Appl. Phys. Lett.* **99**, 032505 (2011).
32. Tusche, C. et al. Quantitative spin polarization analysis in photoelectron emission microscopy with an imaging spin filter. *Ultramicroscopy* **130**, 70–76 (2013).
33. Miyamoto, K. et al. Orbital-symmetry-selective spin characterization of Dirac-cone-like state on W(110). *Phys. Rev. B* **93**, 161403(R) (2016).
34. Bentmann, H. et al. Profiling spin and orbital texture of a topological insulator in full momentum space. *Phys. Rev. B* **103**, L161107 (2021).
35. Maaß, H. et al. Spin-texture inversion in the giant Rashba semiconductor BiTeI. *Nat. Commun.* **7**, 11621 (2016).
36. Suga, S. & Tusche, C. Photoelectron spectroscopy in a wide *hν* region from 6 eV to 8 keV with full momentum and spin resolution. *J. Electron Spectrosc. Relat. Phenom.* **200**, 119–142 (2015).
37. Heide, M., Bihlmayer, G. & Blügel, S. Dzyaloshinskii-Moriya interaction accounting for the orientation of magnetic domains in ultrathin films: Fe/W(110). *Phys. Rev. B* **78**, 140403 (2008).
38. Janak, J. F., Williams, A. R. & Moruzzi, V. L. Local exchange-correlation potentials and the Fermi surface of copper. *Phys. Rev. B* **6**, 4367–4370 (1972).
39. Vosko, S. H., Wilk, L. & Nusair, M. Accurate spin-dependent electron liquid correlation energies for local spin density calculations: a critical analysis. *Can. J. Phys.* **58**, 1200–1211 (1980).
40. Papanikolaou, N., Zeller, R. & Dederichs, P. H. Conceptual improvements of the KKR method. *J. Phys. Condens. Matter* **14**, 2799–2823 (2002).
41. Stefanou, N. & Zeller, R. Calculation of shape-truncation functions for voronoi polyhedra. *J. Phys. Condens. Matter* **3**, 7599–7606 (1991).
42. Stefanou, N., Akai, H. & Zeller, R. An efficient numerical method to calculate shape truncation functions for wigner-seitz atomic polyhedra. *Comput. Phys. Commun.* **60**, 231–238 (1990).
43. Heers, S. Effect of spin-orbit scattering on transport properties of low-dimensional dilute alloys. PhD thesis, RWTH Aachen Univ. (2011).

Acknowledgements

Y.-J.C. and C.T. thank the staff of Elettra for their help and hospitality during their visit in Trieste, and beamline staff M. Jugovac, G. Zamborlini, V. Feyer (PGI-6, FZ-Jülich), and T. O. Menteş (Elettra) for their assistance during the experiment and providing the W(110) crystal. We are indebted to J.-P. Hanke and Y. Mokrousov for discussions. Y.-J.C., C.T., and C.M.S. gratefully acknowledge funding by the BMBF (Grant number 05K19PGA). The authors gratefully acknowledge the computing time granted through JARA on the supercomputer JURECA at Forschungszentrum Jülich.

Author contributions

Y.-J.C. and C.T. carried out the experiment and analyzed the experimental data. M.H. and B.Z. carried out first-principle calculations and analyzed the theoretical data with assistance by G.B. Y.-J.C. drafted the manuscript with assistance by C.T. C.T. designed and coordinated the research together with C.M.S. and S.B. All authors discussed the results and contributed to the manuscript.

Funding

Open Access funding enabled and organized by Projekt DEAL.

Competing interests

The authors declare no competing interests.

Additional information

Supplementary information The online version contains supplementary material available at <https://doi.org/10.1038/s42005-021-00682-5>.

Correspondence and requests for materials should be addressed to Y.-J.C. or C.T.

Peer review information *Communications Physics* thanks Koji Miyamoto and the other, anonymous, reviewer(s) for their contribution to the peer review of this work. Peer reviewer reports are available.

Reprints and permission information is available at <http://www.nature.com/reprints>

Publisher's note Springer Nature remains neutral with regard to jurisdictional claims in published maps and institutional affiliations.



Open Access This article is licensed under a Creative Commons Attribution 4.0 International License, which permits use, sharing, adaptation, distribution and reproduction in any medium or format, as long as you give appropriate credit to the original author(s) and the source, provide a link to the Creative Commons license, and indicate if changes were made. The images or other third party material in this article are included in the article's Creative Commons license, unless indicated otherwise in a credit line to the material. If material is not included in the article's Creative Commons license and your intended use is not permitted by statutory regulation or exceeds the permitted use, you will need to obtain permission directly from the copyright holder. To view a copy of this license, visit <http://creativecommons.org/licenses/by/4.0/>.

© The Author(s) 2021